

Gravitational Bose-Einstein condensation in the kinetic regime

D.G. Levkov,^{1,2,*} A.G. Panin,^{1,2} and I.I. Tkachev^{1,3}

¹*Institute for Nuclear Research of the Russian Academy of Sciences, Moscow 117312, Russia*

²*Moscow Institute of Physics and Technology, Dolgoprudny 141700, Russia*

³*Novosibirsk State University, Novosibirsk 630090, Russia*

We study Bose-Einstein condensation and formation of Bose stars in the virialized dark matter halos/miniclusters by universal gravitational interactions. We prove that this phenomenon does occur and it is described by kinetic equation. We give expression for the condensation time. Our results suggest that Bose stars may form kinetically in the mainstream dark matter models such as invisible QCD axions and Fuzzy Dark Matter.

1. Introduction. Bose stars are lumps of Bose-Einstein condensate bounded by self-gravity [1, 2]. They can be made of condensed dark matter (DM) bosons — say, invisible QCD axions [3] or Fuzzy DM [4]. That is why their physics, phenomenology and observational signatures remain in the focus of cosmological research for decades [5], see recent papers [6, 7]. Unfortunately, formation of Bose stars is still poorly understood and many recent works have to assume their existence.

In this Letter we study Bose-Einstein condensation in the virialized DM halos/miniclusters caused by universal gravitational interactions. We work at large occupation numbers which is correct if the DM bosons are light. Notably, we consider kinetic regime where the initial coherence length and period of the DM particles are close to the de Broglie values $(mv)^{-1}$ and $(mv^2)^{-1}$ and much smaller than the halo size R and condensation time τ_{gr} ,

$$mvR \gg 1, \quad mv^2\tau_{gr} \gg 1. \quad (1)$$

We numerically solve microscopic equations for the ensemble of gravitating bosons in this case and find that the Bose stars indeed form. We derive expression for τ_{gr} and study kinetics of the process.

Up to our knowledge, gravitational Bose-Einstein condensation in kinetic regime has not been observed in simulations before. Old works considered only contact interactions between the DM bosons [8] which are non-universal and suppressed by quartic constants $\lambda \sim 10^{-50}$ [9] and 10^{-100} [10] in models of QCD axions and string axions/Fuzzy DM. Our results show that in these cases gravitational condensation is *faster*: although the Newton's constant Gm^2 is tiny, its effect is enhanced by collective interaction of large fluctuations in the boson gas at large distances, cf. [11].

On the other hand, all previous numerical studies of Bose star formation considered coherent initial configurations of the bosonic field — a Gaussian wavepacket [12] or the Bose stars themselves [13, 14]. A spectacular simulation of structure formation by wavelike/Fuzzy DM [13, 15] started from (almost) homogeneous Bose-Einstein condensate. In all these cases the Bose stars form almost immediately [12, 13] from the lowest-energy part of the initial condensate.

We consider entirely different situation (1) when the DM bosons are virialized in the initial state. The closest

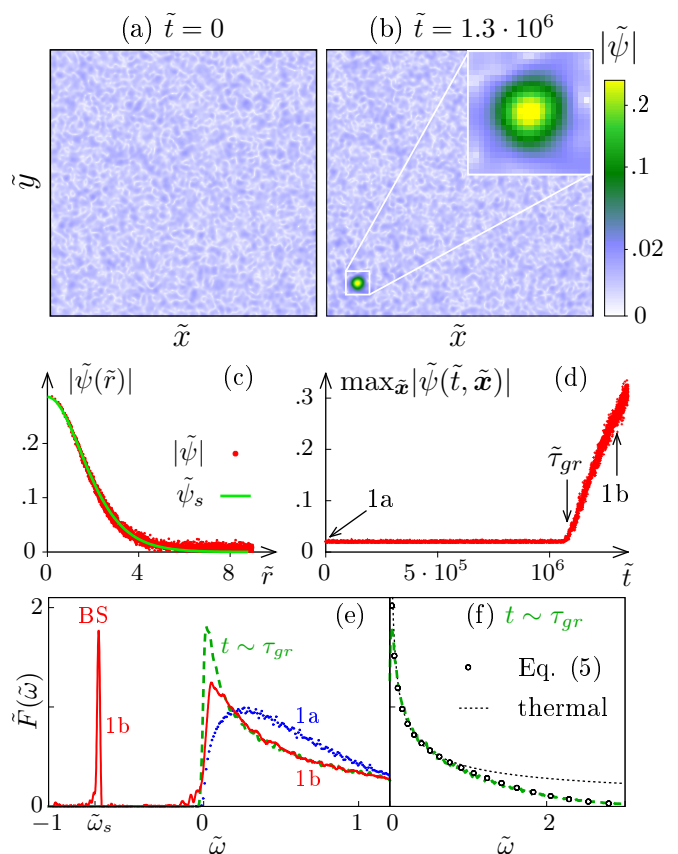


FIG. 1. Formation of Bose star from random field with initial distribution $|\psi_{\tilde{\mathbf{p}}}|^2 \propto e^{-\tilde{\mathbf{p}}^2}$ and total mass $\tilde{N} = 50$ in the box $0 \leq \tilde{x}, \tilde{y}, \tilde{z} < 125$. These values correspond to the center of the axion minicluster with $M_c \sim 10^{-13} M_\odot$ and $\Phi \sim 2.7$ in Sec. 8. (a), (b) Sections $\tilde{z} = \text{const}$ of the solution $|\tilde{\psi}(\tilde{t}, \tilde{\mathbf{x}})|$ at (a) $\tilde{t} = 0$ and (b) $\tilde{t} > \tilde{\tau}_{gr} \approx 1.08 \cdot 10^6$. (c) Radial profile $|\tilde{\psi}(\tilde{r})|$ of the object in Fig. 1b (points) compared to the Bose star $\tilde{\psi}_s(\tilde{r})$ with $\tilde{\omega}_s \approx -0.7$ (line). (d) Maximum of $|\tilde{\psi}(\tilde{\mathbf{x}})|$ over the box as a function of time. (e) Spectra (3) at times 1a, b and at the eve of Bose star nucleation, $\tilde{t} = 1.05 \cdot 10^6 \sim \tilde{\tau}_{gr}$. (f) The spectrum at $t \sim \tau_{gr}$ (dashed line) versus the solution of Eq. (5) (circles) and thermal law $\tilde{F} \propto \tilde{\omega}^{-1/2}$ (dots).

study to ours was performed in [16], but kinetic regime was not achieved there due to computational limitations. Note that we do not consider scenario of [11], where axions form cosmological condensate at the radiation-dominated stage, cf. [17]. Indeed, at realignment the momenta of such axions are comparable to the Hubble scale, and Eq. (1) is violated.

2. *The birth of the Bose star.* Consider N nonrelativistic gravitationally interacting bosons in the periodic box of size L . At large occupation numbers this system is described by a random classical field $\psi(t, \mathbf{x})$ [8] evolving in its own gravitational potential $U(t, \mathbf{x})$,

$$\begin{aligned} i\partial_t\psi &= -\Delta\psi/2m + mU\psi, \\ \Delta U &= 4\pi G m(|\psi|^2 - n), \end{aligned} \quad (2)$$

where the mean particle density $n \equiv N/L^3$ is subtracted in the second line for consistency [15]. Notably, Eqs. (2) simplify in dimensionless variables: substitutions $\mathbf{x} = \tilde{\mathbf{x}}/mv_0$, $t = \tilde{t}/mv_0^2$, $U = v_0^2\tilde{U}$ and $\psi = v_0^2\tilde{\psi}\sqrt{m/G}$ exclude parameters m and G from the equations and reference velocity v_0 — from the initial conditions. The rescaled particle number is $\tilde{N} \equiv \int d^3\tilde{\mathbf{x}} |\tilde{\psi}|^2 = Gm^2N/v_0$.

We fix initial conditions in the momentum space. A representative class of them describes Gaussian-distributed bosons, $|\tilde{\psi}_{\tilde{\mathbf{p}}}|^2 = 8\pi^{3/2}\tilde{N}e^{-\tilde{\mathbf{p}}^2}$, with random phases $\arg\tilde{\psi}_{\tilde{\mathbf{p}}}$, where $\tilde{\mathbf{p}} \equiv \mathbf{p}/mv_0$. Fourier-transforming $\tilde{\psi}_{\tilde{\mathbf{p}}}$, we obtain an isotropic and homogeneous initial configuration $\tilde{\psi}(0, \tilde{\mathbf{x}})$ with minimal coherence length in Fig. 1a. Then we numerically evolve Eqs. (2) using an exceptionally stable 3D algorithm, see Supplemental material S2 and movie [18]. Apart from the erratic motion of ψ -peaks and deeps, nothing happens for a long time $t < \tau_{gr}$, where $\tilde{\tau}_{gr} \sim 10^6$ for the solution in Fig. 1. Then a coherent, compact and spherically-symmetric object appears at $t > \tau_{gr}$, see Fig. 1b. With time the object grows in mass and moves in a Brownian way due to interaction with the fluctuating environment.

To explain what happens, we recall that any interaction between the bosons should lead to thermal equilibrium, and in the case of large occupation numbers — to formation of a Bose-Einstein condensate. Gravitational interaction is not an exception, as pioneering works [11, 16] argued. But then the condensate cannot appear in a homogeneous state [17]. Rather, it should fragment due to Jeans instability into a set of isolated Bose stars, cf. [8], which is therefore the actual end-state of the condensation process.

The field profiles of the isolated Bose stars are found by solving Eqs. (2) with the stationary spherical Ansatz $\psi = \psi_s(r)e^{-i\omega_s t}$, $U = U_s(r)$ at each $\omega_s < 0$, see e.g. [19]. We computed them using a separate code. Results coincide with the profiles of condensed objects on the lattice (see Fig. 1c) thus proving that we indeed observe nucleation of Bose stars. We performed simulations for a large set of parameters, for δ - and θ -like initial dis-

tributions, $|\psi_{\mathbf{p}}|^2 \propto \delta(|\mathbf{p}| - mv_0)$ and $\theta(mv_0 - |\mathbf{p}|)$, in addition to the Gaussian. Every time we observed formation of a Bose star with correct profile $\psi_s(r)$, $U_s(r)$ correct mass $M_s \propto \psi_s^{1/2}(0)$ and correct size proportional to M_s^{-1} , see [19]. Note that the Bose stars nucleate wide and rarefied, then shrink and become dense as they accumulate bosons. Unlike in other studies, no “seed” Bose condensate was present in our simulations at $\tau < \tau_{gr}$, otherwise it would grow above the background in a short time, see Fig. 1d.

3. *The spectrum.* To look deeper into the initial, seemingly featureless stage of gas evolution, we compute distribution $F(t, \omega) = dN/d\omega$ of bosons over energies ω . This quantity equals to Fourier image of the correlator

$$F = \int \frac{dt_1}{2\pi} d^3\mathbf{x} \psi^*(t, \mathbf{x})\psi(t + t_1, \mathbf{x}) e^{i\omega t_1 - t_1^2/\tau_1^2} \quad (3)$$

in kinetic regime $(mv_0^2)^{-1} \ll \tau_1 \ll \tau_{gr}$, see Supplementary material S1 and [20]. In dimensionless calculations we use $\tilde{F} = mv_0^2 F/N$ normalized to unity: $\int \tilde{F} d\tilde{\omega} = 1$, where $\tilde{\omega} = \omega/mv_0^2$.

Figure 1e shows that the spectrum (3) completely changes during evolution at $t < \tau_{gr}$. It starts from a wide bell $\tilde{F} \propto \tilde{\omega}^{1/2} e^{-2\tilde{\omega}}$ corresponding to Gaussian distribution in momenta in Fig. 1a. As the time goes on, F develops a peak at low ω and becomes close to thermal at intermediate energies, $F \propto \omega^{-1/2}$, see the graph at $t \sim \tau_{gr}$ in Figs. 1e and 1f. At high ω it still falls off exponentially, as high-frequency modes thermalize slowly [21]. Once the Bose star nucleates, a small δ -peak appears in the distribution. With time this δ -peak grows in height and shifts to the left, see the spectrum 1b in Fig. 1e. It explicitly shows condensed particles of the same energy $\omega_s < 0$ inside the growing Bose star.

Below we use the δ -peak at $\omega < 0$ as an indicator of Bose star nucleation: we define τ_{gr} as the moment when the peak is twice higher than the fluctuations in $F(t, \omega)$.

4. *Condensation time.* In kinetic regime evolution of $F(t, \omega)$ is described by kinetic equation — this fact can be proven by solving Eqs. (2) perturbatively and using approximations (1), see Supplemental material S1 and cf. [20]. One therefore expects that the time of Bose star formation τ_{gr} is proportional with some coefficient b to the kinetic relaxation time: $\tau_{gr} = 4b\sqrt{2}/(\sigma_{gr}vnf)$, where $\sigma_{gr} \approx 8\pi(mG)^2\Lambda/v^4$ is the transport Rutherford cross section of gravitational scattering, $\Lambda = \log(mvL)$ is the Coulomb logarithm, and $f = 6\pi^2n/(mv)^3 \gg 1$ is the phase-space density that appears due to Bose stimulation [8]. The coefficient $b = O(1)$ accounts for the details of the process. It is expected to depend weakly on the initial distribution.

Taking all factors together, we obtain expression

$$\tau_{gr} = \frac{b\sqrt{2}}{12\pi^3} \frac{mv^6}{G^2n^2\Lambda}, \quad b \sim 1, \quad (4)$$

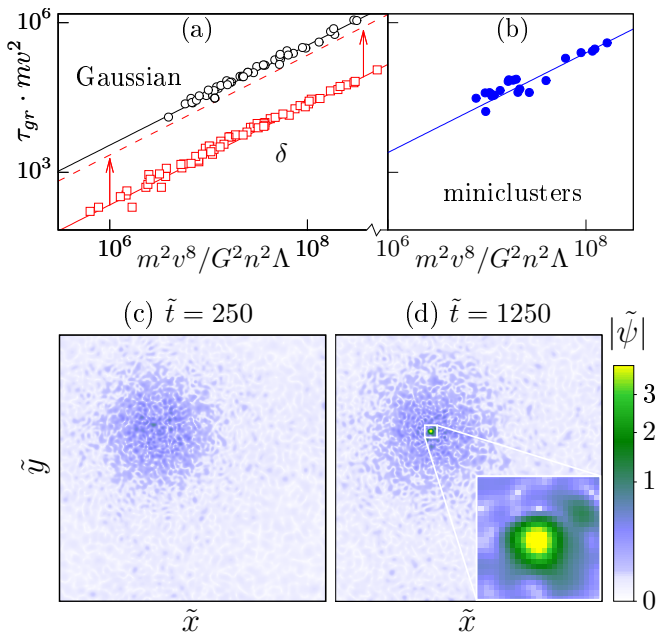


FIG. 2. (a) Time to Bose star formation in the cases of Gaussian (\circ) and δ -peaked (\square) initial distributions. The δ -graphs are shifted downwards ($\tau_{gr} \rightarrow \tau_{gr}/10$) for visualization purposes. Lines depict fits by Eq. (4). (b) The same for isolated miniclusters. (c), (d) Slices $\tilde{z} = \text{const}$ of the solution $|\tilde{\psi}(\tilde{t}, \tilde{\mathbf{x}})|$ describing formation of a Bose star in the center of a minicluster; $\tilde{N} = 290$, $\tilde{L} \approx 63$.

that apart from the Coulomb logarithm Λ involves only local parameters i.e. the boson number density n and characteristic velocity v . So, up to weak logarithmic dependence on the size L formation of the Bose star can be regarded as a local process, with periodic box representing a central part of some DM halo. We will confirm this intuition below.

We performed simulations of the gas with Gaussian initial distribution at different \tilde{L} and \tilde{n} . Our results for τ_{gr} (circles in Fig. 2a) cover two orders of magnitude, but they are nevertheless well fitted by Eq. (4) with $v = v_0$ and $b \approx 0.9$ (upper line in Fig. 2a). To confirm that Eq. (4) is universal, we repeated the calculations for the initial δ -distribution, $|\psi_{\mathbf{p}}|^2 \propto \delta(|\mathbf{p}| - mv_0)$ (squares in Fig. 2a). The new values of τ_{gr} are still described by Eq. (4), albeit with slightly different coefficient $b \approx 0.6$. We conclude that Eq. (4) is a practical and justified expression for the time of Bose star formation.

5. *Kinetics.* Let us show that evolution of $F(t, \omega)$ in Fig. 1e is indeed governed by the Landau kinetic equation [21] for the homogeneous isotropic Coulomb ensemble,

$$\partial_t \tilde{F} = \tau_0^{-1} \partial_{\tilde{\omega}} \left[\tilde{A} \partial_{\tilde{\omega}} \tilde{F} + (\tilde{B} \tilde{F} - \tilde{A}) \tilde{F} / 2\tilde{\omega} \right], \quad (5)$$

see Supplementary material S1.4 for derivation. Here the scattering integral in the right-hand side involves $\tilde{A}(\tilde{\omega}) = \int_0^\infty d\tilde{\omega}_1 \min^{3/2}(\tilde{\omega}, \tilde{\omega}_1) \tilde{F}^2(\tilde{\omega}_1) / (3\tilde{\omega}_1 \tilde{\omega}^{1/2})$,

$\tilde{B}(\tilde{\omega}) = \int_0^{\tilde{\omega}} d\tilde{\omega}_1 \tilde{F}(\tilde{\omega}_1)$, it is explicitly proportional to the inverse relaxation time $\tau_0^{-1} = 8\pi^3 n^2 G^2 (\Lambda + a) / mv_0^6 \sim \tau_{gr}^{-1}$. Notably, Eq. (5) is valid in the leading logarithmic approximation $\Lambda \gg 1$ which is too rough for our numerical solutions with $\Lambda \sim 5$. To get a quantitative comparison, we added an unknown correction $a = O(1)$ to Λ .

We numerically evolve Eq. (5) starting from the same initial distribution as in Fig. 1. In Fig. 1f the solution $F(t, \omega)$ (circles) is compared to the microscopic distribution (3) (dashed line) at $t \approx \tau_{gr}$, where $a \approx 5$ is obtained from the fit. We observe agreement in the kinetic region $\tilde{\omega} \gg 2\pi^2 / \tilde{L}^2$ which confirms Eq. (5) at $t < \tau_{gr}$.

Note that unlike in the case of short-range interactions [22] thermalization in Landau equation does not proceed via power-law turbulent cascades [21], and we do not observe them in Figs. 1e,f. Nevertheless, we think that Eq. (5) provides the basis for analytic description of gravitational Bose-Einstein condensation.

6. *Miniclusters.* So far we assumed that homogeneous ensemble in the box correctly describes central parts of DM halos. Now, we study the isolated halos/miniclusters themselves and verify this assumption. Recall that in large volume nonrelativistic gas forms clumps at scales $R \gtrsim 2\pi/k_J$ due to Jeans instability, where $k_J^2 = 2\pi G n m^2 \langle \omega^{-1} \rangle$ and the average is computed with $F(\omega)$. Starting numerical evolution from the homogeneous ensemble with δ -distributed momenta at $L > 2\pi/k_J$, we indeed observe formation of a virialized minicluster in Fig. 2c. With time it remains stationary until the Bose star appears in its center, see Fig. 2d and movie [18]. Thus, formation of Bose stars is not specific to finite boxes.

We checked that our kinetic expression for τ_{gr} works for the virialized miniclusters. To this end we generated many different miniclusters, computed their central densities n and virial velocities $\langle v^2 \rangle = -2\langle \omega \rangle / m$ using the $\omega < 0$ part of the distribution $F(\omega)$, estimated their radii R . In Fig. 2b we plot the times of Bose star formation in the miniclusters versus these parameters and $\Lambda = \log(mvR)$ (points). The numerical data are well approximated by Eq. (4) with $b \approx 0.7$ (line) although the statistical fluctuations are now larger due to limited control over momentum distribution inside the miniclusters.

Estimating the virial velocity $v^2 \sim 4\pi G m n R^2 / 3$ in the halo of radius R , one recasts Eq. (4) in the intuitively simple form $\tau_{gr} \sim 0.047 (R/v) (Rmv)^3 / \Lambda$, where the numerical factor is computed. Remarkably, τ_{gr} equals to the free-fall time R/v multiplied by the cube of kinetic constant $Rmv \gg 1$ in Eq. (1). In non-kinetic case $Rmv \sim 1$ the Bose stars form immediately [12, 13, 15].

7. *Bose star growth.* After nucleation the Bose stars start to acquire particles from the ensemble. Due to computational limitations we are able to observe only the first decade of their mass increase that proceeds according to the heuristic law $M_s(t) \simeq cv_0(t/\tau_{gr} - 1)^{1/2} / Gm$ with $c = 3 \pm 0.7$. The ratio t/τ_{gr} in this expression sug-

gests that growth of the Bose stars is a kinetic process deserving a separate study.

8. *Discussion.* Let us argue that the Bose stars appear in the popular cosmological models even if we conservatively assume that halos/miniclusters in these models are initially virialized. If the DM is made of invisible QCD axions [3], the smallest substructures are axion miniclusters [23, 24] of typical mass $M_c \sim 10^{-13} M_\odot$ [25]. These miniclusters can be characterized [24] by the ratio $\Phi + 1 \equiv n/\bar{n}|_{RD}$ of their central density n to the cosmological axion density \bar{n} at the radiation-dominated stage when they are still in the linear regime. Substituting their typical parameters [24] into Eq. (4) and expressing the result in terms of Φ and M_c , we find,

$$\tau_{gr} \sim \frac{10^9 \text{ yr}}{\Phi^3(1+\Phi)} \left(\frac{M_c}{10^{-13} M_\odot} \right)^2 \left(\frac{m}{26 \mu\text{eV}} \right)^3,$$

where the reference axion mass is taken from [9]. Thus, typical miniclusters with $\Phi \sim 1$ condense during the lifetime of the Universe, the densest ones with $\Phi \sim 10^3$ [24] — in several hours. The Bose stars are important [6] as they hide a part of DM from observations. After becoming large they may explode into relativistic axions [7] or emit radiophotons via parametric resonance [2] which at different redshifts may explain FRB [26] and anomalies of ARCADE 2 and EDGES [27].

Note that gravitational relaxation of virialized QCD axions is significantly faster than relaxation due to self-coupling $\lambda \equiv m^2/f_a^2$, where $f_a \sim 10^{11}$ GeV is the Peccei-Quinn scale. Indeed, in kinetic regime the relaxation rates are proportional to the cross sections, and $\tau_{self}/\tau_{gr} \sim \sigma_{gr}/\sigma_{self} \sim (10f_a G^{1/2}/v)^4$. In typical miniclusters $v \sim 10^{-10} \ll 10f_a G^{1/2}$, and gravitational interactions win by $\tau_{self}/\tau_{gr} \sim 10^{12}$.

Another popular class of DM models is based on string axions / Fuzzy DM [4]. An interesting though recently constrained [28] scenario considers the smallest mass $m \sim 10^{-22}$ eV of these particles [15] when their de Broglie wavelength inside the dwarf galaxies is comparable to the size of the galaxy cores, $mvR \sim 1$. As we argued, the Bose stars should appear in these cores in free-fall time. This explains their fast formation [15] in numerical simulations. At larger masses one substitutes typical parameters of dwarf satellites into Eq. (4),

$$\tau_{gr} \sim 10^6 \text{ yr} \left(\frac{m}{10^{-22} \text{ eV}} \right)^3 \left(\frac{v}{30 \text{ km/s}} \right)^6 \left(\frac{0.1 M_\odot/\text{pc}^3}{\rho} \right)^2.$$

The Bose stars nucleate there if $m \lesssim 2 \cdot 10^{-21}$ eV, at the boundary of experimentally allowed mass window [28]. Then the missing satellites may hide as Bose stars. At even larger m the Bose stars may form in miniclusters and in cores of large galaxies, they may grow overcritical and explode [7]. Note that self-interaction of typical

string axions [10] with $f_a \sim 10^{-2} G^{-1/2}$ is less effective than gravity because $v \ll 10f_a G^{1/2}$ in all structures.

We thank A. Pustynnikov, D. Gorbunov, M. Ivanov, E. Nugaev and V. Rubakov for discussions. This work was supported by the grant RSF 16-12-10494. Numerical calculations were performed on the Computational cluster of TD INR RAS.

* levkov@ms2.inr.ac.ru

- [1] R. Ruffini, S. Bonazzola, Phys. Rev. **187**, 1767 (1969).
- [2] I. I. Tkachev, Sov. Astron. Lett. **12**, 305 (1986).
- [3] P. Sikivie, Lect. Notes Phys. **741**, 19 (2008).
- [4] A. Ringwald, Phys. Dark Univ. **1**, 116 (2012).
- [5] F. E. Schunck and E. W. Mielke, Class. Quant. Grav. **20**, R301 (2003)
- [6] J. Eby *et al*, JHEP **1612**, 066 (2016). P. S. B. Dev, M. Lindner and S. Ohmer, Phys. Lett. B **773**, 219 (2017). T. Helfer *et al*, JCAP **1703**, 055 (2017). J. Eby *et al*, JHEP **1704**, 099 (2017). E. Braaten, A. Mohapatra and H. Zhang, Phys. Rev. D **96**, 031901 (2017). P.-H. Chavanis, arXiv:1710.06268. L. Visinelli *et al*, Phys. Lett. B **777**, 64 (2018).
- [7] D. G. Levkov, A. G. Panin, and I. I. Tkachev, Phys. Rev. Lett. **118**, 011301 (2017).
- [8] I. I. Tkachev, Phys. Lett. B **261**, 289 (1991). S. Khlebnikov and I. Tkachev, Phys. Rev. D **61**, 083517 (2000).
- [9] V. B. Klaer and G. D. Moore, JCAP **1711**, 049 (2017).
- [10] A. Arvanitaki *et al*, Phys. Rev. D **81**, 123530 (2010).
- [11] P. Sikivie and Q. Yang, Phys. Rev. Lett. **103**, 111301 (2009). O. Erken *et al*, Phys. Rev. D **85**, 063520 (2012).
- [12] E. Seidel, W.-M. Suen, Phys. Rev. Lett. **72**, 2516 (1994). F. S. Guzman and L. A. Urena-Lopez, Astrophys. J. **645**, 814 (2006).
- [13] H.-Y. Schive *et al*, Phys. Rev. Lett. **113**, 261302 (2014).
- [14] B. Schwabe, J. C. Niemeyer and J. F. Engels, Phys. Rev. D **94**, 043513 (2016). M. Bezares, C. Palenzuela and C. Bona, Phys. Rev. D **95**, 124005 (2017).
- [15] H.-Y. Schive *et al*, Nature Phys. **10**, 496 (2014).
- [16] S. Khlebnikov, Phys. Rev. D **62**, 043519 (2000).
- [17] A. H. Guth *et al*, Phys. Rev. D **92**, 103513 (2015).
- [18] https://www.youtube.com/playlist?list=PLMxQF3HFStXO_CFowbYSTkjRv~xZEG-Vn
- [19] P.-H. Chavanis, Phys. Rev. D **84**, 043531 (2011).
- [20] V. Zakharov, V. L'vov, and G. Falkovich, *Kolmogorov Spectra of Turbulence I. Wave Turbulence*, Springer Berlin Heidelberg, 1992.
- [21] V. E. Zakharov, V. I. Karas', Phys. Usp. **56**, 49 (2013).
- [22] D. V. Semikoz and I. I. Tkachev, Phys. Rev. Lett. **74**, 3093 (1995); Phys. Rev. D **55**, 489 (1997).
- [23] C. J. Hogan, M. J. Rees, Phys. Lett. B **205**, 228 (1988).
- [24] E. W. Kolb and I. I. Tkachev, Phys. Rev. Lett. **71**, 3051 (1993); Phys. Rev. D **49**, 5040 (1994); Astrophys. J. **460**, L25 (1996).
- [25] J. Enander, A. Pargner, and T. Schwetz, JCAP **1712**, 038 (2017).
- [26] I. I. Tkachev, JETP Lett. **101**, 1 (2015).
- [27] J. Kehayias, T. W. Kephart and T. J. Weiler, JCAP **1510**, 053 (2015). S. Fraser *et al*, arXiv:1803.03245.
- [28] V. Iršič *et al*, Phys. Rev. Lett. **119**, 031302 (2017). E. Armengaud *et al*, MNRAS **471**, 4606 (2017).

Supplemental material on the article:
Gravitational Bose-Einstein condensation in the kinetic regime

S1. LANDAU EQUATION

Evolution of a random Bose field at large occupation numbers can be well approximated by the classical field theory. Such situations appear, in particular, in systems far from thermal equilibrium when particles have energies much lower than the temperature in the eventual thermal state, $\mathbf{p}^2 \ll 2mT$, see e.g. [S1]. For the period of evolution with this property the seminal ‘‘ultraviolet catastrophe’’ is not threatening the theory and quantum statistics is not needed. This allows us to describe the initial stages of thermalization by solving the classical Schrödinger-Poisson problem (2). In our simulations the energies of all particles at the epoch of Bose star formation are well below the lattice UV cutoff, not to say about the region of parametrically high momenta corresponding to order-one occupation numbers in the thermal ensemble, see Fig. 1f.

Let derive Landau kinetic equation for the gravitating ensemble of random classical waves (2) inside the structure of size R — a halo/minicluster or a periodic box. The main steps of our derivation are standard [20], although specific attention should be paid to kinetic corrections suppressed by powers of $(mvR)^{-2}$ and to infrared divergence of the scattering integral caused by long-range nature of gravitational interactions. Treating these subtleties, we justify Landau approximation for the integral thus supporting the relaxation time estimates from the main text.

S1.1. Vlasov equation

We introduce real Wigner distribution for the ensemble of random classical fields,

$$f_{\mathbf{p}}(\mathbf{x}) = \int d^3\xi e^{-i\mathbf{p}\xi} \langle \psi_{\mathbf{x}+\xi/2} \psi_{\mathbf{x}-\xi/2}^* \rangle, \quad (\text{S1})$$

where $\psi_{\mathbf{x}} \equiv \psi(\mathbf{x})$ and $\langle \cdot \rangle$ is the average with respect to random initial phases of the fields. In the kinetic regime (1) the value of $f_{\mathbf{p}}(\mathbf{x})$ can be interpreted [20] as an occupation number of bosons in the elementary cell $d^3\mathbf{x}d^3\mathbf{p} = (2\pi)^3$.

Taking the time derivative of Eq. (S1) and using Eqs. (2), one obtains dynamical equation for $f_{\mathbf{p}}(\mathbf{x})$,

$$\begin{aligned} \partial_t f + \mathbf{p}\nabla_{\mathbf{x}} f / m \\ = 2m \text{Im} \int d^3\xi e^{-i\mathbf{p}\xi} \langle \psi_{\mathbf{x}+\xi/2} \psi_{\mathbf{x}-\xi/2}^* U_{\mathbf{x}+\xi/2} \rangle, \end{aligned} \quad (\text{S2})$$

where Im extracts ξ -odd part of $U_{\mathbf{x}+\xi/2}$. Note that the

gravitational potential equals

$$U_{\mathbf{x}} = 4\pi Gm \int d^3\mathbf{x}' \Delta_{\mathbf{x}-\mathbf{x}'}^{-1} (|\psi_{\mathbf{x}'}|^2 - n). \quad (\text{S3})$$

Here Δ^{-1} is the Green’s function of the Poisson equation (2): $\Delta\Delta_{\mathbf{x}}^{-1} \equiv \delta^3(\mathbf{x})$ and $\Delta_{-\mathbf{x}}^{-1} = \Delta_{\mathbf{x}}^{-1}$. Thus, Eq. (S2) contains a correlator of four ψ -fields. We should express it via $f_{\mathbf{p}}(\mathbf{x})$ in order to obtain kinetic equation in the closed form.

To this end we exploit weak coupling expansion. Recall that in the initial state ψ is a Gaussian random field, all non-Gaussianities appear later due to small gravitational interactions. This means that the Wick theorem remains approximately valid,

$$\begin{aligned} \langle \psi_{\mathbf{x}_1} \psi_{\mathbf{x}_2}^* \psi_{\mathbf{x}_3} \psi_{\mathbf{x}_4}^* \rangle = \langle \psi_{\mathbf{x}_1} \psi_{\mathbf{x}_2}^* \rangle \langle \psi_{\mathbf{x}_3} \psi_{\mathbf{x}_4}^* \rangle \\ + \langle \psi_{\mathbf{x}_1} \psi_{\mathbf{x}_4}^* \rangle \langle \psi_{\mathbf{x}_3} \psi_{\mathbf{x}_2}^* \rangle + \langle \psi_{\mathbf{x}_1} \psi_{\mathbf{x}_2}^* \psi_{\mathbf{x}_3} \psi_{\mathbf{x}_4}^* \rangle_{\text{conn}}, \end{aligned} \quad (\text{S4})$$

where the connected part $\langle \cdot \rangle_{\text{conn}} \sim O(G)$ is small, it gives $O(G^2)$ contribution into Eq. (S2).

We substitute Eqs. (S3) and (S4) into Eq. (S2) and express all two-point functions via $f_{\mathbf{p}}(\mathbf{x})$, Eq. (S1). This gives non-local equation

$$\begin{aligned} \partial_t f + \mathbf{p}\nabla_{\mathbf{x}} f / m = 2m \text{Im} \bar{U}(\mathbf{x} + \frac{i}{2}\nabla_{\mathbf{p}}) f_{\mathbf{p}}(\mathbf{x}) \\ + \frac{8\pi Gm^2}{(2\pi)^6} \text{Im} \int d^3\{\xi\xi'qq'\} \Delta_{\xi}^{-1} e^{i\xi'q-i\xi q'} \\ \times f_{\mathbf{p}+q}(\mathbf{x} + \frac{\xi}{2}) f_{\mathbf{p}+q'}(\mathbf{x} + \frac{\xi'}{2}) + \text{St} f, \end{aligned} \quad (\text{S5})$$

where $\bar{U}(\mathbf{x}) \equiv \langle U(\mathbf{x}) \rangle$ is the mean potential satisfying

$$\Delta\bar{U} = 4\pi Gm \left(\int \frac{d^3\mathbf{p}}{(2\pi)^3} f_{\mathbf{p}}(\mathbf{x}) - n \right), \quad (\text{S6})$$

and scattering integral $\text{St} f \sim O(G^2)$ represents contribution of the connected correlator in Eq. (S4).

Ignoring $\text{St} f$ in Eq. (S5), one can get an equation for $f_{\mathbf{p}}(\mathbf{x})$ valid to the first order in G and to all orders in the kinetic parameter $(mvR)^{-1}$. This simplification is unacceptable for us, however. First, all terms in Eq. (S5) except for $\text{St} f$ are T -odd: they change sign under the time reflection $f_{\mathbf{p}}(\mathbf{x}) \rightarrow f_{-\mathbf{p}}(-t, \mathbf{x})$. Equation with $\text{St} f = 0$ preserves T -symmetry and cannot describe kinetic relaxation [S2][20], unless some source of irreversibility is provided. Second, as we explain below, all dangerous $O(G)$ terms vanish in the spatially homogeneous box and in the centers spherically-symmetric halo/miniclusters, i.e. in all places where we numerically observe formation of Bose stars. Third, our numerical results suggest that the condensation time scale τ_{gr} is set by $\text{St} f$.

A homogeneous ensemble of random waves in the box is described by \mathbf{x} -independent real distribution $f_{\mathbf{p}}$. In

this case $\bar{U} = 0$ and, also, the imaginary part of the integral in Eq. (S5) vanishes, as one can see by changing $(\boldsymbol{\xi}, \boldsymbol{\xi}') \rightarrow (-\boldsymbol{\xi}, -\boldsymbol{\xi}')$. Equation (S5) takes the form

$$\partial_t f = \text{St } f. \quad (\text{S7})$$

Thus, the time scale τ_{gr} of Bose star formation in the box is determined by the scattering integral explicitly.

Now, consider halo/minicluster of size R . We simplify Eq. (S5) by performing consistent expansion in $(mvR)^{-2} \ll 1$. To this end we note that $f_{\mathbf{p}+\Delta\mathbf{p}}(\mathbf{x}+\Delta\mathbf{x})$ can be Taylor-expanded in $\Delta\mathbf{x} \ll R$ or $\Delta\mathbf{p} \ll mv$ because the halo is almost homogeneous at scales $\Delta\mathbf{x} \ll R$, while the Wigner distribution in Eq. (S1) is insensitive to $\Delta\mathbf{p} \ll mv$ due to exponential falloff of the correlator at distances exceeding the correlation length $(mv)^{-1}$. Performing these Taylor expansions in the respective kinematic domains of the integral in Eq. (S5), one finds,

$$\partial_0 f + \nabla_{\mathbf{p}} h \nabla_{\mathbf{x}} f - \nabla_{\mathbf{x}} h \nabla_{\mathbf{p}} f + S_3 \approx \text{St } f, \quad (\text{S8})$$

where $S_3 = (m/24) \partial_i \partial_j \partial_k \bar{U} \partial_{p_i} \partial_{p_j} \partial_{p_k} f$ reflects uncertainty of order $|\mathbf{p}|^{-1}$ in particle's position, while

$$h_{\mathbf{p}}(\mathbf{x}) = \frac{\mathbf{p}^2}{2m} + m\bar{U}(\mathbf{x}) - \frac{4\pi G m^2}{(2\pi)^3} \int \frac{d^3 \mathbf{k}}{\mathbf{k}^2} f_{\mathbf{p}-\mathbf{k}}(\mathbf{x}) \quad (\text{S9})$$

is one-particle Hamiltonian with gravitational mass defect in the third term. To the leading order Eqs. (S8), (S9) reproduce the celebrated Vlasov equation. They also include two corrections suppressed as $(mvR)^{-2}$: S_3 and the last term in Eq. (S9). We ignored corrections with relative suppression $(mvR)^{-4}$, as they are smaller than $\text{St } f \sim f/\tau_{gr} \sim \partial_t f / (mvR)^3$, see discussion in Sec. 6. Note that kinetic expansion of T -odd $O(G)$ terms in Eq. (S5) goes in powers of $(mvR)^{-2}$, as these terms change sign under $\mathbf{p} \rightarrow -\mathbf{p}$ reflections.

Equation (S8) describes evolution of halos/miniclusters in the regime (1). Its largest second and third terms vanish if the distribution is virialized i.e. given by an arbitrary function of one-particle conserved quantities, e.g. $f = f(h_{\mathbf{p}}(\mathbf{x}))$. Thus, these terms describe fast collisionless mixing rather than thermalization. Small kinetic correction S_3 takes effect at parametrically larger time scales. It conserves spatial densities of mass, energy and momentum at every \mathbf{x} , $\int d^3 \mathbf{p} (\alpha + \beta_i p^i + \gamma p^2/2m) S_3 = 0$, and therefore does not induce transport in the \mathbf{x} -space. Besides, this term becomes negligibly small in the centers of spherically-symmetric miniclusters $r \lesssim (mv)^{-1}$ because $\partial^3 \bar{U}(r) = 0$ at $r = 0$. Thus, it cannot drive kinetic relaxation in the halo centers where we numerically observe formation of Bose stars. This leaves $\text{St } f$ as the only source of condensation.

So, it is natural to expect that the time τ_{gr} of Bose star formation inside the virialized halo/minicluster is determined by the scattering integral. Our numerical results strongly support this viewpoint.

S1.2. Landau scattering integral

Recall that the collision integral $\text{St } f$ is a contribution of the connected correlator $\langle \psi \psi^* U \rangle_{conn}$ into the right-hand side of Eq. (S2). Landau noticed [S2][20] that in the particular case of long-range interactions main fluctuations of the potential $U_{\mathbf{x}}$ are caused by density perturbations at large distances in Eq. (S3),

$$(mv)^{-1} \ll |\mathbf{x}' - \mathbf{x}| \ll R. \quad (\text{S10})$$

Below we will confirm this nontrivial observation and estimate related corrections. In the region (S10) Eq. (S3) admits multipole expansion,

$$U_{\mathbf{x}+\boldsymbol{\xi}/2} \approx U_{\mathbf{x}} + \frac{\boldsymbol{\xi}^i}{2} \partial_i U_{\mathbf{x}} \quad \text{if } |\boldsymbol{\xi}| \lesssim (mv)^{-1}. \quad (\text{S11})$$

Importantly, Eq. (S11) is approximately valid for the fluctuations of U , not just for the smooth mean potential \bar{U} . Then the scattering integral in Eq. (S2) takes the form

$$\text{St } f = -\nabla_{\mathbf{p}} \mathcal{F}, \quad (\text{S12})$$

where the Landau flux

$$s_i = -\frac{4\pi G m^2}{(2\pi)^3} \int d^3 \mathbf{x}' d^3 \mathbf{p}' \mathcal{F}_{\mathbf{x}, \mathbf{p}}^{\mathbf{x}', \mathbf{p}'} \partial_i \Delta_{\mathbf{x}-\mathbf{x}'}^{-1}, \quad (\text{S13})$$

describes diffusion in the phase space. It involves the connected correlator of four fields,

$$\begin{aligned} \mathcal{F} = & \int d^3 \boldsymbol{\xi} d^3 \boldsymbol{\xi}' e^{-i\mathbf{p}\boldsymbol{\xi} - i\mathbf{p}'\boldsymbol{\xi}'} \\ & \times \langle \psi_{\mathbf{x}+\boldsymbol{\xi}/2} \psi_{\mathbf{x}-\boldsymbol{\xi}/2}^* \psi_{\mathbf{x}'+\boldsymbol{\xi}'/2} \psi_{\mathbf{x}'-\boldsymbol{\xi}'/2}^* \rangle_{conn}, \quad (\text{S14}) \end{aligned}$$

where $\langle \cdot \rangle_{conn}$ is a combination of four- and two-point functions introduced in Eq. (S4). Note that the integrals in Eqs. (S14), (S13) are saturated at small $\boldsymbol{\xi} \sim p^{-1}$ and $\boldsymbol{\xi}' \rightarrow 0$.

We treat \mathcal{F} in the same way as f in the previous Section. Acting by ∂_t and using Eqs. (2), we obtain dynamical equation

$$\partial_0 \mathcal{F} + (\mathbf{p} \nabla_{\mathbf{x}} + \mathbf{p}' \nabla_{\mathbf{x}'}) \mathcal{F} / m = \mathcal{A}, \quad (\text{S15})$$

with the right-hand side $\mathcal{A}_{\mathbf{x}, \mathbf{p}}^{\mathbf{x}', \mathbf{p}'}$ containing correlators of six fields $\langle \psi^2 \psi^* U \rangle$ at time t , cf. Eq. (S2). Next, we compute \mathcal{A} to the leading order in G and $(mvR)^{-1}$. Namely, we express it via the two-point functions f like in Eq. (S4), but ignore all connected parts. We also use the dipole approximation (S11) and expand $f_{\mathbf{p}}(\mathbf{x})$ in small variations of \mathbf{p} and \mathbf{x} whenever possible. We find,

$$\mathcal{A} = 4\pi G m^2 \partial_j \Delta_{\mathbf{x}-\mathbf{x}'}^{-1} \left[f'^2 \partial_{p_j} f - f^2 \partial_{p_j} f' \right], \quad (\text{S16})$$

where $f' = f_{\mathbf{p}'}(\mathbf{x}')$ and $f = f_{\mathbf{p}}(\mathbf{x})$. Note that \mathcal{A} in Eq. (S16) vanishes at large separations $|\mathbf{x} - \mathbf{x}'| \gtrsim R$ because either \mathbf{x} or \mathbf{x}' in this case is outside of the halo.

The solution of Eq. (S15) is,

$$\mathcal{F} = \int_{-\infty}^t dt' \mathcal{A}_{\mathbf{x}+\mathbf{p}(t'-t)/m, \mathbf{p}}^{\mathbf{x}'+\mathbf{p}'(t'-t)/m, \mathbf{p}'} \Big|_{t'}, \quad (\text{S17})$$

where we recalled that \mathcal{F} vanishes in the beginning of the process. In the region (S10) this solution simplifies. First, the left-hand side of Eq. (S15) suggests that \mathcal{F} responds to the external source \mathcal{A} at time scales $t - t' \sim |\mathbf{x} - \mathbf{x}'|/v$. Thus, we can limit integration in Eq. (S17) to the region $(mv^2)^{-1} \ll t - t' \ll R/v$ corresponding to Eq. (S10). Then all f 's in the integrand can be taken at time t . Second, $f' \approx f_{\mathbf{p}'}(\mathbf{x})$, $f \approx f_{\mathbf{p}}(\mathbf{x})$ in Eq. (S17) because the shifts of their spatial arguments are small in the region (S10). After these approximations \mathbf{x}' and t' enter only the argument of the Green's function in Eq. (S16).

Substituting Eqs. (S16), (S17) into Eq. (S13), one arrives at the Landau flux [S2],

$$s_i = \frac{G^2 m^4}{4\pi^2} \int d^3 \mathbf{p}' \Pi_{ij}(\mathbf{u}) \left[f^2 \partial_{p'_j} f' - f'^2 \partial_{p_j} f \right], \quad (\text{S18})$$

where $\mathbf{u} = (\mathbf{p} - \mathbf{p}')/m$ is the relative velocity of the interacting waves and we denote $f \equiv f_{\mathbf{p}}(\mathbf{x})$, $f' \equiv f_{\mathbf{p}'}(\mathbf{x})$,

$$\Pi_{ij} = 8\pi \int dt'' d^3 \mathbf{y} \partial_i \Delta_{\mathbf{y}}^{-1} \partial_j \Delta_{\mathbf{y}+u\mathbf{t}''}^{-1}, \quad (\text{S19})$$

and $\mathbf{y} \equiv \mathbf{x} - \mathbf{x}'$, $t'' \equiv t' - t$.

The last step is to compute Π_{ij} in Eq. (S19). Spherical symmetry gives $\Pi_{ij} = \Pi_1(u)\delta_{ij} + \Pi_2(u)u^i u^j$. Besides,

$$u^j \Pi_{ij} = 8\pi \int d^3 \mathbf{y} \Delta_{\mathbf{y}}^{-1} \partial_i \Delta_{\mathbf{y}}^{-1} = 0, \quad (\text{S20})$$

$$\delta^{ij} \Pi_{ij} = -\frac{2}{|\mathbf{u}|} \int_{-R/v}^{-(mv^2)^{-1}} \frac{dt''}{t''} = \frac{2}{|\mathbf{u}|} \log(mvR),$$

where in the first line we used $u^j \partial_j = \partial_{t''}$. In the second line we integrated by parts, then substituted $\Delta_{\mathbf{x}}^{-1} = -(4\pi|\mathbf{x}|)^{-1}$. This leaves divergent integral over t'' which is logarithmically sensitive to the boundaries of the Landau region $(mv^2)^{-1} \ll |t''| \ll R/v$. We obtain,

$$\Pi_{ij} = \Lambda (u^2 \delta_{ij} - u_i u_j) / u^3, \quad (\text{S21})$$

where $\Lambda \equiv \log(mvR)$ and $u \equiv |\mathbf{u}|$.

Expressions (S12), (S18), (S21) give Landau scattering integral in its canonical form. Note that the relaxation time estimate from the main text can be drawn directly from these expressions, cf. [8]. Indeed, trading the p -derivatives for $(mv)^{-1}$, integral over momentum for $V_p \sim 4\pi m^3 v^3 / 3$, using $u \sim v\sqrt{2}$ and $f \sim (2\pi)^3 n / V_p$, one obtains $\text{St } f \sim f / \tau_{gr}$, where τ_{gr} is given by Eq. (4).

Now, let us discuss corrections to the Landau integral related to wave scattering at very small and very

large distances, $|\mathbf{x} - \mathbf{x}'| \lesssim (mv)^{-1}$ and $|\mathbf{x} - \mathbf{x}'| \sim R$. In the former case one can Fourier-transform Eq. (S3) introducing momentum transfer \mathbf{q} conjugate to $\mathbf{x} - \mathbf{x}'$. Scattering processes with $|\mathbf{q}| \gg mv$ do not occur because waves of such high momenta are absent in the ensemble. Thus, true scattering integral has a cutoff at $q^{-1} \sim |\mathbf{x} - \mathbf{x}'| \gtrsim (mv)^{-1}$ that regularizes logarithmic divergence at small $|t''|$ in Eq. (S20). A similar cutoff at $v|t''| \sim |\mathbf{x} - \mathbf{x}'| \gtrsim R$ is related to the fact that matter is absent outside of the halo/minicluster. Clearly, uncontrolled contributions from the regions near the cutoffs are comparable to the Landau scattering integral, but have $O(1)$ constants in front instead of the Coulomb logarithm $\Lambda \equiv \log(mvR)$. Thus, Landau approximation keeps terms proportional to $\Lambda \gg 1$ and ignores relative $O(1)$ corrections. In Sec. 5 we treat these corrections heuristically, by changing $\Lambda \rightarrow \Lambda + a$, where $a \sim O(1)$. In Fig. 1f we demonstrate that Landau equation with $a \approx 5$ correctly describes evolution of the distribution function.

It is worth noting that the traditional Boltzmann integral also has logarithmic accuracy in $\Lambda \gg 1$ in the case of isolated halo/minicluster. Indeed, it diverges logarithmically [20] at small momentum transfers $\mathbf{q} \rightarrow 0$ due to long-range nature of gravitational interactions. Unsuppressed contributions at $|\mathbf{q}| \sim R^{-1}$ correspond to interactions at distances of order of the structure size. Imposing cutoff at these scales, one recovers finite result up to uncontrolled $O(1)$ terms. This situation is drastically different from the case of electromagnetic plasma where the Coulomb interactions disappear at distances larger than the microscopic Debye length $\lambda_D \ll R$ which regularizes the Boltzmann integral [S2].

S1.3. Energy distribution

Let us argue that Eq. (3) gives distribution of bosons over energies in the kinetic regime (1): $F(t, \omega) \approx dN/d\omega$. On the one hand, this expression involves average over large time interval $\tau_1 \gg (mv^2)^{-1}$ which is equivalent to the ensemble average due to ergodic hypothesis: $F \approx \langle F \rangle$. On the other hand, we consider regime where at time scales $\tau_1 \ll \tau_{gr}$ the mean potential $\bar{U}(\mathbf{x})$ is almost static and the field ψ evolves in this potential. Thus, $\psi \approx \sum_n c_n \psi_n(\mathbf{x}) e^{-i\omega_n t}$, where $\psi_n(\mathbf{x})$ are the eigenstates of \bar{U} with almost time-independent eigenenergies ω_n , while $|c_n|^2$ are the occupation numbers. Substituting this form into Eq. (3), we obtain,

$$F \approx \sum_n \langle |c_n|^2 \rangle \delta_{\tau_1}(\omega - \omega_n), \quad (\text{S22})$$

where $\delta_{\tau_1} = (\tau_1/2\sqrt{\pi}) e^{-\tau_1^2(\omega - \omega_1)^2/4}$ is a sharply-peaked function indistinguishable from $\delta(\omega - \omega_n)$ at energy resolution $\Delta\omega \gtrsim \tau_1^{-1}$. Thus, for chosen values

$\tau_1^{-1} \ll mv^2 \sim \omega$ the function F gives distribution of particles over energies $dN/d\omega$.

S1.4. Homogeneous isotropic ensemble

Finally, we derive kinetic equation (5) for the homogeneous spherically-symmetric ensemble of random classical waves evolving in the box of size L , cf. [20]. In this case f_p depends only on $p = |\mathbf{p}|$ and the Landau flux \mathbf{s} is collinear with momentum, $\mathbf{p}\mathbf{s} = ps$. Equations (S7), (S12), (S18) give,

$$\partial_t f = \frac{2G^2 m^5}{\pi p^2} (\Lambda + a) \partial_p [A \partial_p f + B f^2], \quad (\text{S23})$$

where we computed the angular integrals and introduced $A = \int_0^\infty p' dp' \min(p^3, p'^3) f'^2 / 3p$, $B = \int_0^p p' f' dp'$. In Eq. (S23) we included the heuristic parameter a from Sec. S1.2.

Now, we express f_p in terms of the energy distribution $F(\omega)$. Since $dN = F d\omega = 4\pi p^2 L^3 f_p dp / (2\pi)^3$, we have,

$$F(\omega) = mL^3 p f_p / 2\pi^2, \quad \omega = p^2 / 2m.$$

Substituting this expression into Eq. (S23), we find,

$$\begin{aligned} \partial_t F &= \frac{2}{\pi} G^2 m^3 (\Lambda + a) \\ &\times \partial_\omega [A \partial_\omega F + (2\pi^2 B F / mL^3 - A) F / 2\omega], \end{aligned} \quad (\text{S24})$$

where

$$\begin{aligned} A(\omega) &= \frac{4\pi^4}{3mL^6} \int_0^\infty d\omega' \min^{3/2}(\omega, \omega') F'^2 / \omega' \omega^{1/2}, \\ B(\omega) &= \frac{2\pi^2}{L^3} \int_0^\omega d\omega' F' \end{aligned}$$

are the same quantities as in Eq. (S23).

The final step is to introduce dimensionless energy $\tilde{\omega} = \omega / mv_0^2$ and rescaled distribution $\tilde{F} = mv_0^2 F / N$ normalized to unity: $\int_0^\infty d\tilde{\omega} \tilde{F} = 1$. We obtain Eq. (5) with $\tilde{A} = m^2 v_0^2 A / 4\pi^4 n^2$, $\tilde{B} = B / 2\pi^2 n$. Note that the kinetic time scale $\tau_0 \sim \tau_{gr}$ is explicit in Eq. (5) because all physical parameters are scaled out of this equation.

S2. NUMERICAL METHOD

We perform numerical studies using 6-th order pseudo-spectral operator-splitting method [S3] which is unitary, stable, T -symmetric, symplectic, and therefore exceptionally suitable for long statistical simulations. In what follows we explain the method, illustrate its properties and estimate the numerical errors.

Recall that general solution to the Schrödinger equation (2) has the form $\psi(t + \Delta t) = \hat{U} \psi(t)$, where

$$\hat{U} = T \exp \left\{ -i \int_t^{t+\Delta t} dt' \left[\frac{\hat{\mathbf{p}}^2}{2m} + mU(t', \mathbf{x}) \right] \right\},$$

α	1	2	3	4
c_α	$w_3/2$	$(w_2 + w_3)/2$	$(w_1 + w_2)/2$	$(w_0 + w_1)/2$
d_α	w_3	w_2	w_1	w_0

$$\begin{aligned} c_{9-\alpha} &= c_\alpha, \quad d_{8-\alpha} = d_\alpha, \quad d_8 = 0, \quad \sum c_\alpha = \sum d_\alpha = 1, \\ w_0 &= 1 - 2(w_1 + w_2 + w_3), \quad w_1 = -1.17767998417887, \\ w_2 &= 0.235573213359359, \quad w_3 = 0.784513610477560. \end{aligned}$$

TABLE I. Parameters in Eq. (S25).

is a quantum propagator and $\hat{\mathbf{p}} \equiv -i\nabla_{\mathbf{x}}$. The method of [S3] replaces this propagator with discrete formula

$$\hat{U} = \prod_{\alpha=1}^8 e^{-im d_\alpha \Delta t U_\alpha(\mathbf{x})} e^{-ic_\alpha \Delta t \hat{\mathbf{p}}^2 / 2m} + O(\Delta t^7), \quad (\text{S25})$$

where the product is ordered right-to-left, its parameters c_α, d_α are given in Table I, and the potentials U_β are computed using the ‘‘current’’ field, i.e. $\psi(t)$ multiplied by all operators with $\alpha \leq \beta$. Geometrically, Eq. (S25) breaks the time interval Δt into two sets of sub-intervals $\{c_\alpha \Delta t, d_\alpha \Delta t\}$, where each set is symmetric with respect to the central point $t + \Delta t / 2$. ‘‘Kinetic’’ and ‘‘potential’’ propagators are used for the c - and d -sub-intervals, respectively. We stress that Eq. (S25) is valid for our time-dependent potential $U(t, \mathbf{x})$.

Numerical application of Eq. (S25) is straightforward. One introduces cubic uniform lattice with N_x^3 sites at $\mathbf{x} = \mathbf{n}_x \Delta x$, where $\Delta x \equiv L / N_x$ and $0 \leq n_x^i < N_x$. Typically, we use $N_x = 128$ or 256 , and switch to $N_x = 512$ for resolution tests. We store the values of the fields $\psi(\mathbf{x})$, $U(\mathbf{x})$ at the lattice sites.

Time evolution of $\psi(\mathbf{x})$ is calculated by sequentially acting with operators in Eq. (S25). We start by performing the Fourier transform,

$$\psi_{\mathbf{p}} = \Delta x^3 \sum_{\mathbf{x}} \psi(\mathbf{x}) e^{-i\mathbf{p}\mathbf{x}}, \quad (\text{S26})$$

where the momenta $\mathbf{p} = 2\pi \mathbf{n}_p / L$ are discrete, $-N_x / 2 < n_p^i \leq N_x / 2$, due to periodic boundary conditions $\psi(\mathbf{x} + L\mathbf{n}') = \psi(\mathbf{x})$. We apply Eq. (S26) using FFT algorithm with GPU acceleration [S4]. After that multiplication by the rightmost operator in Eq. (S25) corresponds to phase rotation $\psi_{\mathbf{p}} \rightarrow \psi_{\mathbf{p}} e^{-ic_1 \Delta t \mathbf{p}^2 / 2m}$. We return ψ to the coordinate representation with the inverse Fourier transform. Next, we solve the Poisson equation (2) in the momentum space,

$$U_{1, \mathbf{q}} = -4\pi m G |\psi^2|_{\mathbf{q}} / \mathbf{q}^2, \quad U_{1, \mathbf{q}=0} = 0, \quad (\text{S27})$$

where $|\psi^2|_{\mathbf{q}}$ is the Fourier image of $(|\psi(\mathbf{x})|^2 - n)$ calculated via Eq. (S26). Finding $U_1(\mathbf{x})$ from the inverse Fourier transform, we act by the ‘‘potential’’ propagator, i.e. change $\psi(\mathbf{x}) \rightarrow \psi(\mathbf{x}) e^{-im d_1 \Delta t U_1(\mathbf{x})}$. We continue

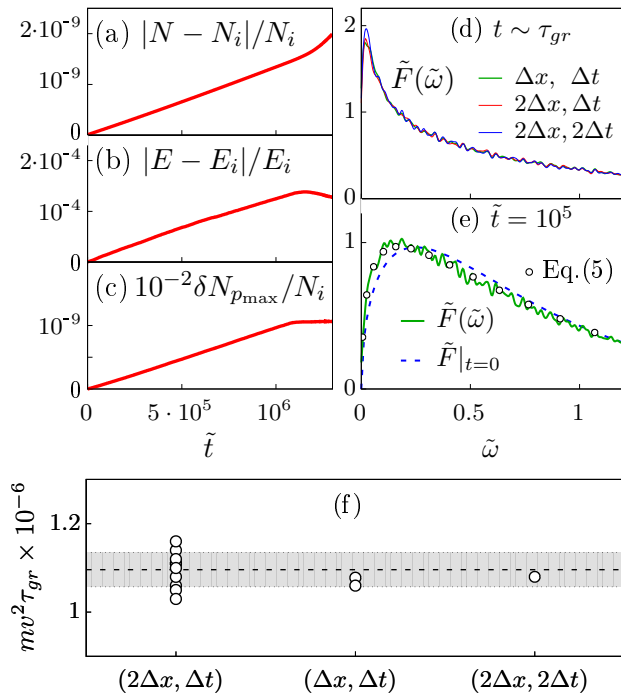


FIG. S1. Tests of the numerical solution in Fig. 1 which is computed on 256^3 lattice with $\Delta\tilde{t} \sim 1.5$, $\Delta\tilde{x} \approx 0.5$. (a), (b) Drift of the particle number N and energy E from their initial values N_i , E_i . (c) Discretization error estimate. (d) Spectra computed at $\tilde{t} = 1.05 \cdot 10^6 \sim \tilde{\tau}_{gr}$ with different space and time resolutions. (e) Spectrum at $\tilde{t} = 10^5$, $\Delta\tilde{t} \sim 0.5$ versus Eq. (5). (f) The time of Bose star formation τ_{gr} at different space and time resolutions, where Δt and Δx are the parameters of the original solution.

to act by operators in Eq. (S25) on $\psi_{\mathbf{p}}$ or $\psi(\mathbf{x})$ until $\psi(t + \Delta t)$ is found.

Let us illustrate advantages of the above numerical method and estimate related errors.

1. Exact conservation of the particle number.

One notes that the Fourier transform (S26) and subsequent multiplication by phases do not change the particle number

$$N = \Delta x^3 \sum_{\mathbf{x}} |\psi(\mathbf{x})|^2 = L^{-3} \sum_{\mathbf{p}} |\psi_{\mathbf{p}}|^2, \quad (\text{S28})$$

which therefore conserves up to round-off errors. Hence, one expects relative change $\Delta N/N \lesssim 2^{-52} N_x^{3/2} \sim 10^{-12}$ during one time step, where we stick to double-precision numbers and $N_x = 256$. In practice we observe even better conservation: the total drift of $N(t)/N_i$ does not exceed 10^{-8} even for our longest runs with 10^6 time steps, see Fig. S1a. Thus, particles do not appear from nowhere in our numerical system.

2. Time resolution.

We use adaptive step size Δt which is chosen to enforce conservation of energy

$$E = L^{-3} \sum_{\mathbf{p}} \frac{p^2}{2m} |\psi_{\mathbf{p}}|^2 + \Delta x^3 \sum_{\mathbf{x}} \frac{m}{2} U(\mathbf{x}) |\psi(\mathbf{x})|^2$$

between t and $t + \Delta t$ with accuracy $\Delta E/E \leq 2 \cdot 10^{-10}$. This corresponds to values $\Delta\tilde{t} \sim 0.1 \div 1.5$ in our $O(\Delta t^6)$ scheme. As a consequence, relative non-conservation of energy in our solutions never exceeds 10^{-3} , see Fig. S1b.

Time resolution of the solutions is proportional to $\Delta E/E$. We estimate it explicitly by performing two steps $\Delta t/2$ instead of one step Δt for a given $\psi(t, \mathbf{x})$. Changes in $\psi(t + \Delta t, \mathbf{x})/n^{1/2}$ are of order $10^{-6} \sim 10^3 \Delta E/E$. Below we show, by drastically increasing and decreasing the time step, that this resolution is good enough to make numerical results independent of Δt .

Note that evolution of the waves with high momentum \mathbf{p} is correctly described by Eq. (S25) that exactly reproduces fast oscillations with frequency $\mathbf{p}^2/2m$. Errors in Δt stem from the ‘‘potential’’ propagators with bounded $\tilde{U}\Delta\tilde{t} \ll 10^{-2}$.

3. Discretization errors.

To estimate effects due to spatial discretization, we consider inverse Fourier transform in the box,

$$\psi(\mathbf{x}) = L^{-3} \sum_{\mathbf{p}} \psi_{\mathbf{p}} e^{i\mathbf{p}\mathbf{x}}. \quad (\text{S29})$$

This representation would be exact if the sum over $\mathbf{p} = 2\pi\mathbf{n}_p/L$ was infinite. But in fact, it has a cutoff at $p_{max} = \pi/\Delta x$. Hence, discretization errors are determined by $|\psi_{p_{max}}|$. One estimates error in the particle number, Eq. (S28), as $\delta N_{p_{max}} \sim p_{max}^3 |\psi_{p_{max}}|^2 / 6\pi^2$. Relative changes in Eqs. (S27), (S25) due to p_{max} are proportional to this quantity. Thus, we can relate the discretization errors to $\delta N_{p_{max}}/N$.

In Fig. S1c we demonstrate that solutions with $N_x = 256$ have $\delta N_{p_{max}}/N \lesssim 10^{-7}$. We independently estimated the discretization errors by performing one time step on 256^3 and 512^3 lattices. Changes in $\psi(t + \Delta t, \mathbf{x})/n^{1/2}$ were smaller than 10^{-9} , which makes spatial resolution at one time step of order $10^{-2} \delta N_{p_{max}}/N$. When performing the calculations, we never allowed this combination to grow above 10^{-8} .

One explains exceptionally good spatial resolution using the spectrum at $t \sim \tau_{gr}$ in Fig. 1f. The central part of this spectrum is close to the power-law $F \propto \omega^{-1/2}$, which changes to exponential falloff in the region $\tilde{\omega} \gtrsim 1.5$. As a consequence, $F \propto p|\psi_{\mathbf{p}}|^2$ is exponentially small at the cutoff frequency $\omega_{max} = p_{max}^2/2$, where $\tilde{\omega}_{max} \approx 21$ for the solution in Fig. 1f. Note that with time the central power-law region of the distribution spreads to higher and lower ω . Eventually, it should hit the cutoff frequency. However, way before that it reaches $\omega \approx 0$ at $t = \tau_{gr}$, and the Bose star is formed. Thus, our numerical solutions correctly describe the initial stages of thermalization, and related discretization errors are exponentially small at $t \lesssim \tau_{gr}$.

We remark that spatial resolution at smaller \tilde{L} and the same $N_x = 256$ is orders of magnitude better than in Fig. S1. We will use this property below.

4. Stability. In general, good resolutions in time and space are not sufficient to reproduce correct statistical properties of the wave ensemble at large time scales $\tilde{t} \sim 10^6$. The main property for that is stability, i.e. absence of exponentially growing or decaying numerical Lyapunov exponents in addition to the ones that are already present in the continuous system. It is well-known that pseudo-spectral methods like ours are exceptionally stable because they exactly conserve symplectic form [S3] and as a consequence, the phase volume

$$\Omega = \prod_{\mathbf{x}} d\psi_{\mathbf{x}} d\psi_{\mathbf{x}}^* = \prod_{\mathbf{p}} \frac{d\psi_{\mathbf{p}} d\psi_{\mathbf{p}}^*}{(L\Delta x)^3}, \quad \Omega(t + \Delta t) = \Omega(t),$$

where ψ and ψ^* are the canonical variables in field theory, while $d\psi(t, \mathbf{x})$ is the difference of two close solutions within the statistical ensemble. Note that conservation of Ω under Eq. (S25) can be demonstrated directly by using $2d\psi_{\mathbf{x}} d\psi_{\mathbf{x}}^* = d|\psi_{\mathbf{x}}|^2 d\arg \psi_{\mathbf{x}}$ and recalling that U depends only on $|\psi_{\mathbf{x}'}|^2$.

The above property means that Eq. (S25) replaces continuous Hamiltonian evolution with symplectic discrete analog, where the Liouville theorem remains satisfied. Practice shows that this precludes appearance of numerical instabilities or exponentially growing errors in conserved quantities, see [S3] and references therein.

5. Independence of the lattice parameters. Let us explicitly verify that statistical properties of our system are not sensitive to Δx and Δt . In Fig. S1d we demonstrate that energy distributions $F(\omega)$ at $t \sim \tau_{gr}$ coincide for solutions computed with different Δt , Δx , and the same initial distribution at $t = 0$. Similarly, Fig. S1f shows that changes in τ_{gr} due to different choices of Δt and Δx are smaller than statistical fluctuations of this quantity related to random initial state; the standard deviation of τ_{gr} is shown with the gray strip on this graph. Thus, our numerical method is stable, while spatial and time resolutions are small enough to make numerical results insensitive to lattice parameters.

6. Exact time-reversibility. Formation of Bose stars is an irreversible process. These objects appear in all of our $\sim 10^3$ solutions and never disappear, their masses grow monotonically with time. Let us argue that this effect is physical i.e. unrelated to accumulation of numerical errors. To this end we note that Eq. (S25) has exact time-reversal symmetry: applying it with time step $-\Delta t < 0$, one reproduces all stages of the algorithm in reverse order. Moreover, the latter operation is equivalent to substitution $\psi \rightarrow \psi^*$ followed by evolution with positive Δt . Thus, irreversible numerical errors can be related only to small round-off effects.

Figure S2a explicitly demonstrates time-reversibility of our numerical code. It shows maximal value of $|\psi(\mathbf{x})|$ within the box as a function of time for the solution which forms a Bose star at $\tilde{\tau}_{gr} \approx 1650$, see Figs. S2b,c. At $t > \tau_{gr}$ the maximal density $|\psi(\mathbf{x})|^2$ corresponds to

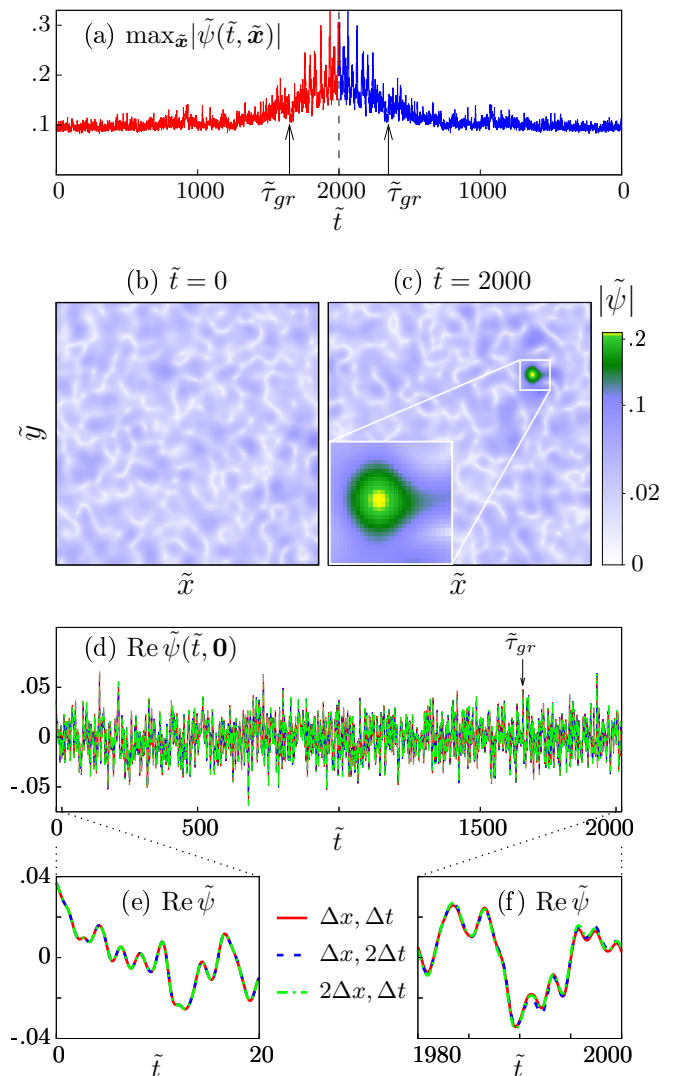


FIG. S2. Tests of the numerical solution with $\tilde{L} = 14\pi$, $\tilde{N} = 55$ and initial distribution $|\psi_{\mathbf{p}}|^2 \propto \delta(|\mathbf{p}| - mv_0)$; in this case $\tilde{\tau}_{gr} \approx 1650$. The reference solution is computed on 256^3 lattice with uniform time step $\Delta \tilde{t} = 0.01$ and $\Delta \tilde{x} \approx 0.2$. (a) Maximum of $|\tilde{\psi}(\tilde{\mathbf{x}})|$ over the box as a function of time. Two parts of the graph correspond to direct evolution to $\tilde{t} = 2000$ followed by evolution with steps $(-\Delta \tilde{t})$ to $\tilde{t} = 0$. (b), (c) Sections $z = \text{const}$ of the solution at $\tilde{t} = 0$ and $\tilde{t} = 2000$. (d) Time evolution of $\text{Re } \tilde{\psi}(\mathbf{x} = 0)$. Coinciding lines of different color represent solutions with different resolutions in space and time. Intervals $0 < \tilde{t} < 20$ and $1980 < \tilde{t} < 2000$ are amplified in the insets (e), (f).

the Bose star center, it increases with time due to growth of this object. At $\tilde{t} = 2000$ we flip $\Delta t \rightarrow -\Delta t$ and continue simulation until $t = 0$ is reached, again. Although all accumulated numerical errors remain in the system, our solution in Fig. S2a correctly describes time-reversed dynamics: density of the Bose star decreases, and this object dissolves in the wave ensemble. We stress that the second part of Fig. S2a is statistically improbable, we

never observed anything like that in the ordinary simulation runs.

We conclude that small round-off errors in our code are not responsible for the irreversible processes of Bose star formation.

7. Continuum limit. One usually does not consider continuum limit of solutions in large-scale statistical simulations such as ours or e.g. N -body simulation. Indeed, evolution of interacting classical systems is intrinsically unstable. It leads to exponentially fast separation of solutions with different Δx and Δt and therefore precludes direct evaluation of the limit $\Delta t, \Delta x \rightarrow 0$ even at moderately large t . Nevertheless, numerical errors have negligible effect on the results of such simulations. Indeed, they mimic small statistical fluctuations in the random system and therefore do not show up in averages. In Fig. S1d,f we explicitly verified this property — demonstrated that $F(\omega)$ and τ_{gr} are not sensitive to Δt and Δx . This is sufficient to show that the statistical simulations are correct.

Nevertheless, our high-precision numerical code gives a unique opportunity to demonstrate explicitly that Bose star formation occurs in the continuum limit. To this end we consider the solution in Fig. S2 which is computed with the best possible time and space resolutions of order 10^{-13} . This means that the numerical solutions with different Δx and Δt coincide at every lattice point with relative precision 10^{-13} at the very first time step, see Figs. S2d,e. The difference between these solutions, however, grows exponentially with time, becomes of order 10^{-3} at $t = \tau_{gr}$ and reaches 5% at $\tilde{t} = 2000$, see

Fig. S2f. Thus, within the interval $0 < \tilde{t} < 2000$ all these solutions are close to the continuum limit. They explicitly prove that the Bose star is formed at $\tilde{\tau}_{gr} \approx 1650$ in the continuum system.

Note that the solution in Fig. S2 confirms our kinetic formula (4) for τ_{gr} : it is represented by the leftmost lower square in Fig. 2. Let us verify the time scales τ_{gr} of other solutions — say, the one in Figs. 1, S1. To this end we repeat the simulation using smaller time steps $\Delta \tilde{t} = 0.25$ and 0.5 , and lattices 256^3 , 512^3 . At $\tilde{t} < 10^5$ all these solutions coincide at all lattice points with relative precision better than 10^{-2} . Hence, they are close to the continuous limit within this time interval. In Fig. S1e we plot their energy distribution $F(\omega)$ at $\tilde{t} = 10^5$. It coincides with the solution to the kinetic equation (5) (points in Fig. S1f) thus confirming the time scale $\tau_0 \approx \tau_{gr}$ in this equation. Recall that our numerical solutions with lower resolution equally well coincide with solution to Eq. (5), see Fig. 1f. Thus, τ_{gr} is correctly computed in the main text.

In this Section we demonstrated that our numerical solutions correctly describe evolution of the gravitating field, and our results are not sensitive to the lattice parameters.

* levkov@ms2.inr.ac.ru

- [S1] S. Y. Khlebnikov and I. I. Tkachev, Phys. Rev. Lett. **77**, 219 (1996).
- [S2] E.M. Lifshitz, L.P. Pitaevskii, *Physical Kinetics. Course on theoretical physics, Vol. 10*. Pergamon Press, 1981.
- [S3] H. Yoshida, Phys. Lett. A **150**, 262 (1990).
- [S4] <http://docs.nvidia.com/cuda/cufft/index.html>